



Multi-frame, ultrafast, x-ray microscope for imaging shockwave dynamics

DANIEL S. HODGE,^{1,*}  ANDREW F. T. LEONG,² SILVIA PANDOLFI,³ KELIN KURZER-OGUL,⁴ DAVID S. MONTGOMERY,² HUSSEIN ALUIE,^{4,5} CINDY BOLME,² THOMAS CARVER,⁶ ERIC CUNNINGHAM,³  CHANDRA B. CURRY,^{3,7} MATTHEW DAYTON,⁸ FRANZ-JOSEPH DECKER,³ ERIC GALTIER,³ PHILIP HART,³ DIMITRI KHAGHANI,³  HAE JA LEE,³ KENAN LI,³  YANWEI LIU,³  KYLE RAMOS,² JESSICA SHANG,^{5,6} SHARON VETTER,³ BOB NAGLER,³ RICHARD L. SANDBERG,¹  AND ARIANNA E. GLEASON³

¹Brigham Young University, Department of Physics and Astronomy, Provo, UT, 84602, USA

²Los Alamos National Laboratory, Los Alamos National Laboratory, Los Alamos, NM, 87545, USA

³SLAC National Accelerator Laboratory, 2575 Sand Hill Rd, Menlo Park, CA, 94025, USA

⁴University of Rochester, Department of Mechanical Engineering, Rochester, NY, 14627, USA

⁵University of Rochester, Laboratory for Laser Energetics, Rochester, NY, 14623, USA

⁶Stanford University, Stanford Nano Shared Facilities, 348 Via Pueblo, Stanford, CA, 94305, USA

⁷University of Alberta, Department of Electrical and Computer Engineering, Edmonton, Alberta T6G 1H9, Canada

⁸Advanced hCMOS Systems, 6300 Riverside Plaza Ln Suite 100, Albuquerque, NM, 87107, USA

*danielhodge42@gmail.com

Abstract: Inertial confinement fusion (ICF) holds increasing promise as a potential source of abundant, clean energy, but has been impeded by defects such as micro-voids in the ablator layer of the fuel capsules. It is critical to understand how these micro-voids interact with the laser-driven shock waves that compress the fuel pellet. At the Matter in Extreme Conditions (MEC) instrument at the Linac Coherent Light Source (LCLS), we utilized an x-ray pulse train with ns separation, an x-ray microscope, and an ultrafast x-ray imaging (UXI) detector to image shock wave interactions with micro-voids. To minimize the high- and low-frequency variations of the captured images, we incorporated principal component analysis (PCA) and image alignment for flat-field correction. After applying these techniques we generated phase and attenuation maps from a 2D hydrodynamic radiation code (xRAGE), which were used to simulate XPCI images that we qualitatively compare with experimental images, providing a one-to-one comparison for benchmarking material performance. Moreover, we implement a transport-of-intensity (TIE) based method to obtain the average projected mass density (areal density) of our experimental images, yielding insight into how defect-bearing ablator materials alter microstructural feature evolution, material compression, and shock wave propagation on ICF-relevant time scales.

© 2022 Optica Publishing Group under the terms of the [Optica Open Access Publishing Agreement](#)

1. Introduction

In inertial confinement fusion (ICF) experiments, such as the recent 1.3 MJ record shot at the National Ignition Facility (NIF) [1], high-energy lasers were converted to x-rays via a hohlraum and were used to compress a fuel capsule. These laser beams ablated the capsule's external layer, which turns into a plasma and quickly compresses the fusion fuel to extreme pressures via shock waves. Analyzing the physical and chemical modifications in ablator materials containing voids at extreme conditions on the micron and nanosecond scales is crucial for advancing ICF, inertial fusion energy (IFE) research and theoretical models [2–5]. Multiple experiments

have indicated that yield degradation arises by growth of hydrodynamic instabilities, such as the Rayleigh-Taylor and Richtmeyer-Meshkov instabilities, at the fuel-ablator interface [6–11]. Specifically, experiments conducted at the NIF, have suggested that one of the main causes of these instabilities are micro-voids in the ablator, which induce a jet of material from the ablator surface, negatively influencing the capsule's performance and prevent attainment of the pressures and densities required to initiate thermonuclear ignition [12,13]. Therefore, to understand how voids contribute to the seeding and growth of hydrodynamic instabilities, we dynamically image void-shock interactions at the nanosecond timescale at 9 keV in a direct-imaging geometry (see Section 2).

Our experiment utilized a high-intensity laser to compress a hollow silica shell void embedded in SU-8 photoresist [14]. To capture the evolution of the shock front as it propagates through a sample, we combined the x-ray free electron laser (XFEL) four-pulse mode at the LCLS and the Icarus V2, an ultrafast x-ray imager (UXI) camera, to obtain four frames of a single sample undergoing ablation-driven shock-compression. These images are captured over an 8 ns time frame [15–20], a unique capability that has the potential to revolutionize dynamic imaging for high-energy density physics (HEDP) experiments and other experiments studying ultrafast phenomena [20]. Previous experiments only had the capability of capturing one or two dynamic frames, which limited the analysis of sample evolution [21–26]. However, with the Icarus V2 detector, images are collected in sequence with greater temporal fidelity, providing a complete picture of the sample's dynamic evolution. In this work, we demonstrated the capabilities of this experimental approach in characterizing void-shock interaction in extreme conditions. Our data provides a movie displaying distinctive features arising from a void-shock interaction and compression with 700 nm spatial resolution.

Flat-field correction (FFC) is performed to normalize against spatial variations in the x-ray beam profile and artifacts accumulated along the x-ray beam. This is important in improving visualization of features in the sample, but also for extracting quantitative areal density information. To account for the stochastic nature of the XFEL beam we developed a FFC approach combining PCA [27] and image alignment [28,29]. The former accounts for variations in the x-ray pulse intensity profile and normalizes against it, while the latter accounts for motion of artifacts induced by the varying x-ray pulse energy. We applied our FFC technique to single XFEL pulse images of shock-compressed micro-voids and visually compare these images with its simulated counterpart using phase and attenuation maps generated from a 2D radiation hydrodynamic code (xRAGE). Finally, we employed a TIE based approach to recover the mass density averaged along the x-ray direction (i.e. areal density). In the remainder of this paper, this will be referred to as the "average mass density map" (areal density) of the sample as it is compressed [30,31]. The comparison between simulations and measured mass density advances our understanding of seeding and growth of hydrodynamic instabilities caused by micro-void compression initiated by a laser-driven shockwave.

This paper is organized as follows: In Section 2, we briefly discuss the experimental design using a high-intensity long-pulse laser to shock-compress a sample containing a void. Then, we describe the UXI camera and its capability in capturing void-shock dynamics with high temporal resolution. In Section 3, we discuss the challenges of imaging void-bearing samples in the holographic regime and discuss the limit of different configurations in visibility of features behind the shock front. We introduce a direct-imaging approach which can improve visualization of void collapse and simplify extraction of mass density compared to the holographic regime. In Section 4, we introduce our FFC algorithm to reduce random fluctuations from the XFEL pulses and lens defects in our images. We compare our FFC images to simulated XPCI images to gain qualitative understanding of void-shock interactions and instability growth. Finally, we show our retrieved mass distribution between successive frames as a shockwave propagates through a void, yielding insight into void-shock interaction. The primary purpose of this work is to

demonstrate a novel experimental platform to capture multiple *in situ* images of a single sample over nanosecond timescales. This technique can be applied to the study of micro-void collapse upon laser-driven shock-compression, which understanding is key to advancing ICF science, as well as other ultrafast phenomena.

2. Experimental setup for direct x-ray imaging

In this proof of principle experiment, we used SU-8 photoresist and hollow silica microspheres as proxy for the ablator material and the voids, respectively. SU-8 [32] was an ideal choice since it has similar properties and shock response to traditional ICF ablators and provides a homogeneous layer and lateral wall quality essential for uniform shock propagation and dynamic x-ray imaging. Hollow silica microspheres were used as proxy for voids and provide several advantages such as their size reproducibility, cost reduction, and time saved compared to other fabrication methods. Additional information about the selected materials and the fabrication techniques used for this experiment and its impact on future HEDP experiments is detailed by Pandolfi et al. [14].

Prior to the experiment, accurate tuning of the fabrication procedure enabled precise and consistent placement of the voids within the SU-8 material for our desired experimental geometry. Figure 1 shows a schematic view of our experimental setup, which are detailed in the following section.

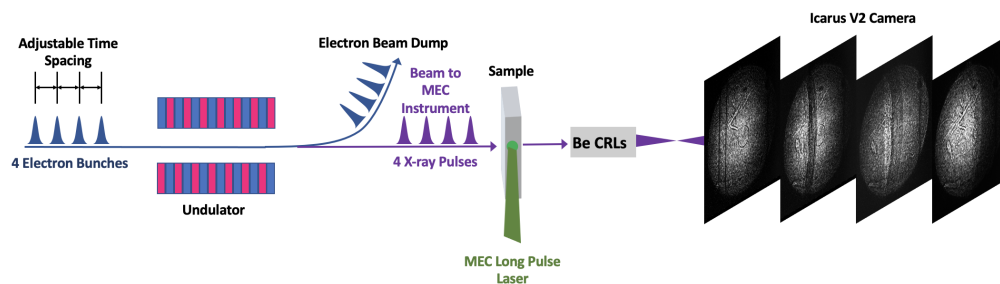


Fig. 1. A schematic describing the direct-imaging setup and the pulse separation for the XFEL four-pulse train at LCLS. Four pulses are sent in at the same time as a laser shockwave interacts with our sample. The Icarus V2, an ultrafast x-ray imaging camera, captures four frames of this single sample during compression.

2.1. High-intensity long-pulse laser for shock compression

Delivery of a laser shockwave to our samples required the 60J, Nd:glass laser system located at the MEC at LCLS [21,22]. This laser provided high-energy pulses at 527 nm [21] with a 10 ns flat-top profile. High energy pulses were delivered as the summed contribution of four separate arms, depicted in Fig. 2(a). The intensity of the pulses varied up to 5% between dynamic shots, but feedback diagnostics were implemented to correct pulse variability.

The drive laser was used to compress a 42 micron diameter hollow silica shell (2.65 g/cm^3 as given by Cospheric LLC, USA) embedded within SU-8 photoresist material (1.2 g/cm^3 [33]). The four laser amplifier arms were focused down to a $150 \text{ }\mu\text{m}$ spot size, delivering a pulse energy of 76.2 J to the sample. The temporal profile for this dynamic run is shown in Fig. 2(a). Figures 2(b) and 2(c) display our beam geometry and the dimensions of our sample ($2.5 \text{ mm} \times \sim 150\text{-}160 \text{ }\mu\text{m} \times 400 \text{ }\mu\text{m}$) as viewed along different beam paths, which are perpendicular to each other. These sample dimensions were designed such that edge effects were not an important factor during void-shock compression. Figure 2(b) shows a $25 \text{ }\mu\text{m}$ thick Kapton layer and 300 nm aluminum layer that were added to the sample to act as ablator and heat-shield, respectively, and to provide a reflective layer for the velocimetry diagnostic. An electro-optic modulator temporally

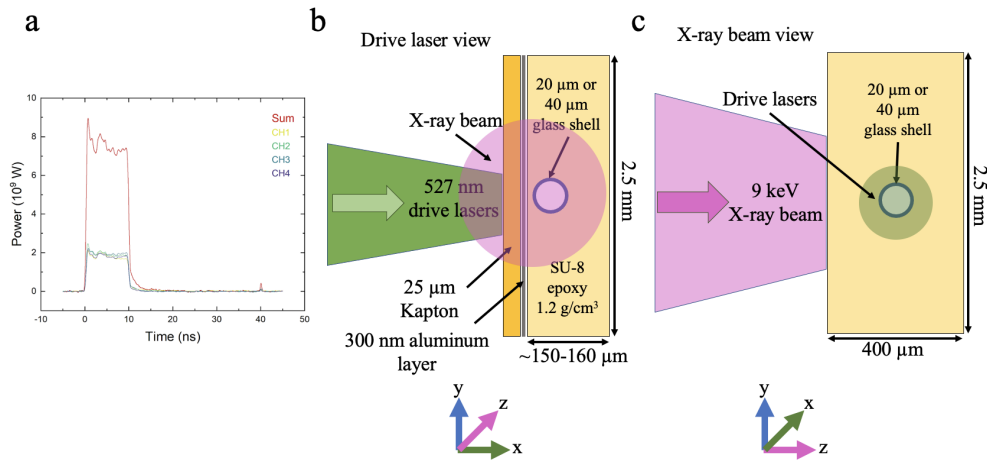


Fig. 2. Panel (a) is the oscilloscope trace of the void-shock dynamic run for the X493 experimental campaign. The energy delivered to the sample by each arm (denoted by colors yellow, green, blue, and purple) is nearly identical, summed to give us the red solid line, a 10 ns flat-top pulse. Panel (b) displays our target schematic of fabricated void samples with laser drive orientation. The corresponding dimensions are given for the different layers. Additionally, the dimensions for the SU-8 sample is given (height of 2.5 mm and $\sim 150\text{-}160\ \mu\text{m}$ thick along the drive laser path). Panel (c) shows a rotated view of panel (b), displaying the dimension of the sample along the z-direction ($400\ \mu\text{m}$ thick along the x-ray propagation direction). Colored axes are given below each target schematic to indicate the drive (green) and x-ray (purple) path directions. The x-ray probe is perpendicular to the shock propagation direction. **Note:** The schematics drawn in panels (b) and (c) are not drawn to scale, but are meant to give a general understanding of our experimental geometry.

manipulated the laser pulses to generate the ideal flat-top shape, reducing inhomogeneous energy delivery to our samples.

By collecting multiple frames from a single shock-compressed sample, we could directly visualize the propagation of the shock front through the sample. Since the time interval between each frame is fixed by the XFEL four-pulses temporal profile and the images were spatially calibrated, it was possible to directly measure U_s , i.e., the shock-wave velocity for each consecutive frame. Using the measured values for U_s and the polyimide equation of state [34], we could infer the pressure attained during shock compression, as well as monitor eventual acceleration or decelerations in the shock-wave propagation due to interference with the void.

2.2. XFEL nanosecond pulse train imaging

In the XFEL multi-pulse mode, we illuminated our samples with a series of four pulses with pulse widths of 40-80 fs and pulse separation of $\sim 2\text{-}4$ ns to create a movie of micro-void compression at the micron length scale (see the bottom row of Fig. 3). The XFEL spot size on target was $300\ \mu\text{m}$, providing a large field of view to visualize the shock front as it propagated through the void. We calibrated this spot size by using a copper 2000 mesh TEM grid. An x-ray microscope was employed to image in the direct-imaging regime, which comprised of 52 beryllium compound refractive lenses (CRLs) ($50\ \mu\text{m}$ radius of curvature and $300\ \mu\text{m}$ aperture) placed 130 mm downstream of the sample. This enabled a magnification of 40X and an effective pixel size of 700 nm. These parameters remained the same for the duration of this experiment. We analyzed how the material structure is altered at and around the micro-void location and how the structure

behaves during compression. This setup was previously demonstrated in PCI geometry with the lenses upstream of the sample [35].

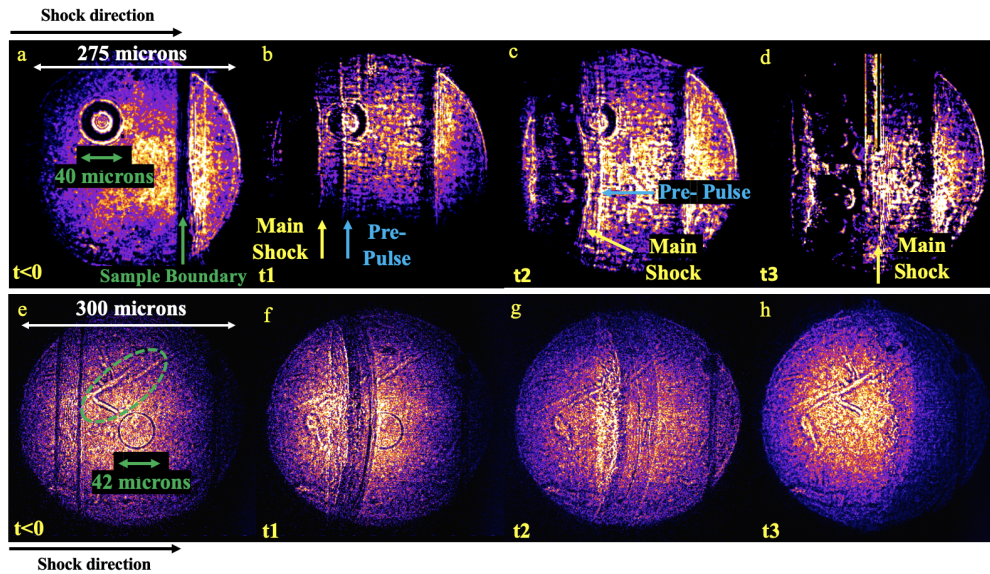


Fig. 3. Each row shows data acquired from a single sample during shock-compression using two different imaging setups and techniques. **Top row(a-d):** LV08 experimental campaign at LCLS. Four x-ray phase contrast images (holographic regime with XFEL energy at 8.23 keV) of a hollow 40 μm diameter void embedded in SU-8 material undergoing laser shock compression collected using the Icarus V2 [35]. A 10 ns flat-top shock wave was delivered to this sample, which is indicated by a yellow arrow in frames b, c, and d. Behind the shock front (left to the yellow arrow) is a dark band, i.e. features that cannot be imaged in this geometry due to strong refraction effects due to the phase-contrast imaging geometry and lower photon energy. **Bottom row(e-h):** X493 experimental campaign at LCLS. Four x-ray images acquired in direct-imaging configuration (XFEL energy at 9 keV), showing a 42 μm diameter void in SU-8 material undergoing laser shock compression. A 10 ns flat-top pulse was delivered to this sample and the void-shock interaction is easily visible compared to the images displayed in the top row. The green dashed line encircles a Be lens blemish in frame e that is not part of the sample.

2.3. Icarus V2 - ultrafast x-ray imager

A critical element that is required for nanosecond imaging is the Icarus V2, an ultrafast x-ray imaging (UXI) camera. We stationed the Icarus V2 detector 4.3 m downstream of the sample at the end of a vacuum flight tube to capture four magnified images of a single sample during laser shock compression. Although four frames were recorded, the last frame was not considered in our dynamic runs since it had consistently low x-ray intensity. This resulted in a low signal-to-noise-ratio that prevented analysis of the data. Therefore, we only include the first three frames captured on the UXI camera, which are presented together with the static frame acquired before the compression occurs (see Fig. 3).

LCLS's capability of delivering several ultrashort, highly coherent x-ray pulses has enabled simultaneous high spatial and temporal resolution that was previously unachievable [20,35–41]. The accelerator at LCLS has the potential of delivering a pulse train up to 8 bunches with a minimum bunch separation of 350 ps [20]. With the advent of the UXI camera these pulse

structures can be exploited to capture up to four images separated by $\sim 2\text{--}4$ ns, paving the way to understanding material dynamics in extreme states at the micron and nanosecond scale.

Sandia National Laboratories (SNL) developed the Icarus V2 for the study of HEDP experiments that occur on ultrafast time scales [15–20]. The Icarus V2 is a burst mode style imager that is 1024×512 pixels with $25 \mu\text{m}$ pixel pitch [15–17,20]. This fast-gated hybrid complimentary metal oxide semiconductor (hCMOS) detector can simultaneously provide multiframe 2D images and temporal information on nanosecond time scales, comparable to the time evolution needed in ICF experiments [15–17]. hCMOS imagers overcome many of the existing limitations in previous imagers [15,16], providing a wider dynamic range and on-device storage of 4 frames per pixel, over 0.5 million pixels, a full well capacity of 600k electrons for each pixel, sensitivity to both soft and hard x-rays, and gate times of ~ 1.5 ns [15–17].

The Icarus V2 has adjustable timing modes available and the exposure time is defined by the readout integrated circuit (ROIC), which is described in detail by Hart et al. and Claus et al. [15,16,20]. One constraint for this camera is that a minimum integration time per frame of 2 ns is required. For this experiment we ran the Icarus V2 in the 1-2 timing mode with an effective signal integration time of 700 ps every 3 ns. This enabled us to capture \sim ns snapshot images of void-shock evolution. More information about the timing modes for the UXI detector is described by Hart et al. [20]. For this experimental campaign the time separation between pulses captured by the UXI was 2.1 ns, 3.85 ns, 2.1 ns. To avoid readout speed limitations, metal-oxide-semiconductor field-effect transistor (MOSFET) switches are used as electronic shutters or gates, which controls the pixel integration time and gain [15,16,20]. These frames are stored on in-pixel storage elements and the images are read off on a slower time scale [15,16,20]. For our readout system we incorporated readout hardware and software from Lawrence Livermore National Laboratory (LLNL) into the LCLS Data Acquisition System (DAQ). Additionally, standard LCLS tools [42] were used for initial image correction (i.e. image geometry alignment and background subtraction). The capabilities of the UXI camera are illustrated in Fig. 3(b)-d, where we visualize the shock propagating through a hollow SiO_2 void embedded in SU-8.

3. Results: Comparison of XPCI imaging in the holographic and direct-imaging regime under shock compression

Propagation-based x-ray phase-contrast imaging (XPCI) uses quasi-coherent x-rays to illuminate a sample while a detector is placed a sufficient distance away to record Fresnel fringes formed by interference between scattered and unscattered x-rays [43–45]. Compared to conventional radiography, this imaging modality enhances the contrast of weakly absorbing objects, such as the shock front and void. Furthermore, compared to other XPCI imaging modalities such as analyzer-based XPCI and x-ray interferometry [46,47], it can use all of the available photons for illumination. These properties are particularly advantageous for photon-starved regimes, such as in ultrafast x-ray imaging. When performing propagation-based XPCI, an important parameter to consider is the Fresnel number

$$Fr = \frac{a^2}{\lambda L}, \quad (1)$$

where a is the size of the object illuminated, λ is the wavelength, and L is the distance from the sample to the detector. This number dictates how much phase-contrast is introduced into the image. When $Fr \approx 1$, also known as the holographic regime, features in the image are significantly enhanced by phase-contrast. In a previous experiment we imaged at $Fr \approx 1$, operating at 8.23 keV and capturing a series of phase-contrast images of void-shockwave interaction by combining the four-pulse train at LCLS with laser shock compression [35]. The XPCI data collected using the UXI camera (field of view (FOV) $275 \mu\text{m}$) are displayed in the top row of Fig. 3. In this experiment a laser shockwave propagated through our sample with a U_s of 10 km/s, resulting in a pressure of ~ 50 GPa. This was the first demonstration at an XFEL where the Icarus V2

was implemented to capture multiple frames, giving insight into how voids affect shock front evolution and overall ablator performance [35].

However, Fig. 3 (top row) shows strong phase-contrast in the form of a dark band, visible in the regions behind the shock front, obstructing our view of the void-shock interaction. To verify the origin of the dark band, we compared our experimental data with simulated XPCI images [35], confirming that imaging at 8.23 keV in the holographic regime obscures the dense region behind and along the shock front [35]. To reduce the amount of phase contrast, we employed a direct-imaging geometry in another void-shock experiment at 8.28 keV and captured a single static and dynamic image of void-shock evolution using the Andor Zyla camera, a single frame detector with $6.5 \mu\text{m}$ pixel pitch. A collection of parameters for this experiment and the others are contained in Table 1 in the Supplement 1. Switching to the direct imaging regime for this experiment involved moving the stack of Be CRLs (25 lenses) from upstream to downstream of the sample. The magnification was 20X for this particular experiment. This placement effectively reduced the sample-to-detector propagation distance and consequently increased $Fr > 1$. This is also known as the near-field regime. Images captured in this regime are displayed in Fig. 4. The orange arrow included in Fig. 4(b) and Fig. 4(c) is included to denote the shock front. The phase-contrast effects are significantly reduced in this configuration in comparison to the images in the top row of Fig. 3, demonstrating the superiority of the direct-imaging configuration. Although the Andor Zyla camera provides a higher spatial resolution, it cannot capture the dynamics with the same temporal fidelity as the UXI camera. Even though a single dynamic image can give significant insights into void collapse, this limitation to a single frame restricts our ability to fully grasp how void-shock interactions evolve on ICF-relevant time scales.

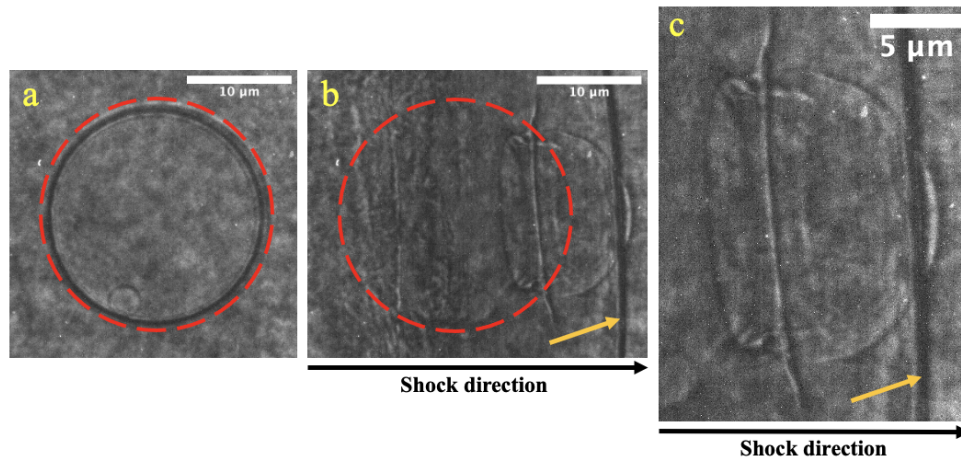


Fig. 4. Panel (a): Static image of a hollow void (SiO_2) that is $20 \mu\text{m}$ in diameter with a FOV of $100 \mu\text{m}$. This void is embedded in SU-8 material. The red circle indicates the location of the void to track its displacement in panel (b). **Panel (b):** Dynamic image where a high-intensity long-pulse laser compresses the void. The dashed red circle displays how much the void has shifted compared to the initial image in panel (a). The orange arrow points to the shock front after it has nearly propagated through the void. **Panel (c):** Zoomed in image of the void from panel (b) for better visibility of the void features and shock front. For emphasis, the orange arrow points to the shock front. **Note:** These single frame static (panel (a)) and dynamic images (panel (b)) were acquired in the X437 experimental campaign. They were captured with a single frame detector, the Andor Zyla, which has a higher pixel pitch ($6.5 \mu\text{m}$) as compared to the faster UXI camera with $25 \mu\text{m}$ pixel pitch.

In our current experimental campaign we adopted this direct imaging configuration and combined it with the UXI camera using the parameters detailed in Section 2.2. The effectiveness of this direct-imaging approach with the UXI detector is demonstrated in the bottom row of Fig. 3, in which laser-driven shock compression was captured by a scintillator-based UXI detector. A comparison between the top and bottom row of Fig. 3 illustrates how the direct-imaging geometry is suited for the task of uncovering details in the shock front over multiple frames while providing a sufficient image contrast-to-noise ratio.

As seen in Fig. 3(g), after the interaction with the compression wave, the void's edge appears at a different position, further within the sample compared to its initial rest position. The void's edge appears to be in front of the shock front itself, which suggests that the shock wave accelerates as it traverses the void, dragging its edges at a higher speed with respect to the surrounding SU-8 material; this "jetting" is expected, as the impedance mismatch between the SU-8 and the air should result in an increase of U_s . Thus, the data demonstrates that the interaction with inhomogeneities within the sample, in this case a micron-sized void, can affect the shock wave propagation, eventually resulting in jetting and possibly giving rise to other instabilities.

The use of the direct-imaging geometry clearly enhances our ability to capture features behind the shock-wave and to provide sufficient phase contrast to visualize without overshadowing the interaction of the shock front with the embedded voids. Although XPCI imaging in the holographic regime is a useful experimental technique for a variety of applications, direct-imaging provides an alternative way to visualize features within or behind the shock front, from the dense compressed region. Moreover, this configuration still enables imaging of ultrafast dynamics at the nanosecond time scale [48].

4. Analysis: Flat-field correction, xRAGE simulation comparison, and mass density extraction

4.1. Flat-field correction (FFC) techniques

For x-ray imaging experiments, FFC is a necessary requirement for image analysis since image quality is degraded by fixed-pattern noise on the detector and random noise from the XFEL pulses, a characteristic that naturally occurs from the XFEL self-amplified spontaneous emission (SASE) mode [49]. FFC is a technique utilized to mitigate image artifacts arising from variations in detector sensitivity and distortions in the optical path not caused by the sample [50]. Conventionally, FFC is computed by first obtaining two sets of images, namely, a series of images with only the beam illuminating the detector (white fields, no sample) and a series of images without any beam illumination (dark fields). Once these images are obtained, a sample is normalized with the average white field image after the average dark field image is computed and subtracted from each white field image. Ideally, this standard calibration procedure reduces fixed-pattern noise and intensity variations in the x-ray beam before the sample, resulting in sample-induced only intensity variations. However, due to the large intensity fluctuations on a shot-to-shot basis due to the stochastic nature of the XFEL, more advanced FFC methods must be used to estimate each pulse's flat field contribution. The ineffectiveness of conventional FFC compared to other methods is displayed in the second row of Fig. 5. We test the performance of principal component analysis [27] combined with image alignment to generate flat-field corrected images where conventional flat-field techniques based on average illumination fail.

4.1.1. Principal component analysis (PCA)

To overcome the problem of fluctuating intensity between frames for FFC, we implemented PCA demonstrated by Hagemann et al. [27], which is a dimensionality reduction or feature extraction technique that reduces the dimensionality of large data sets so they can be more easily interpreted and information loss is minimized [27,51–53]. Dimensionality is reduced by

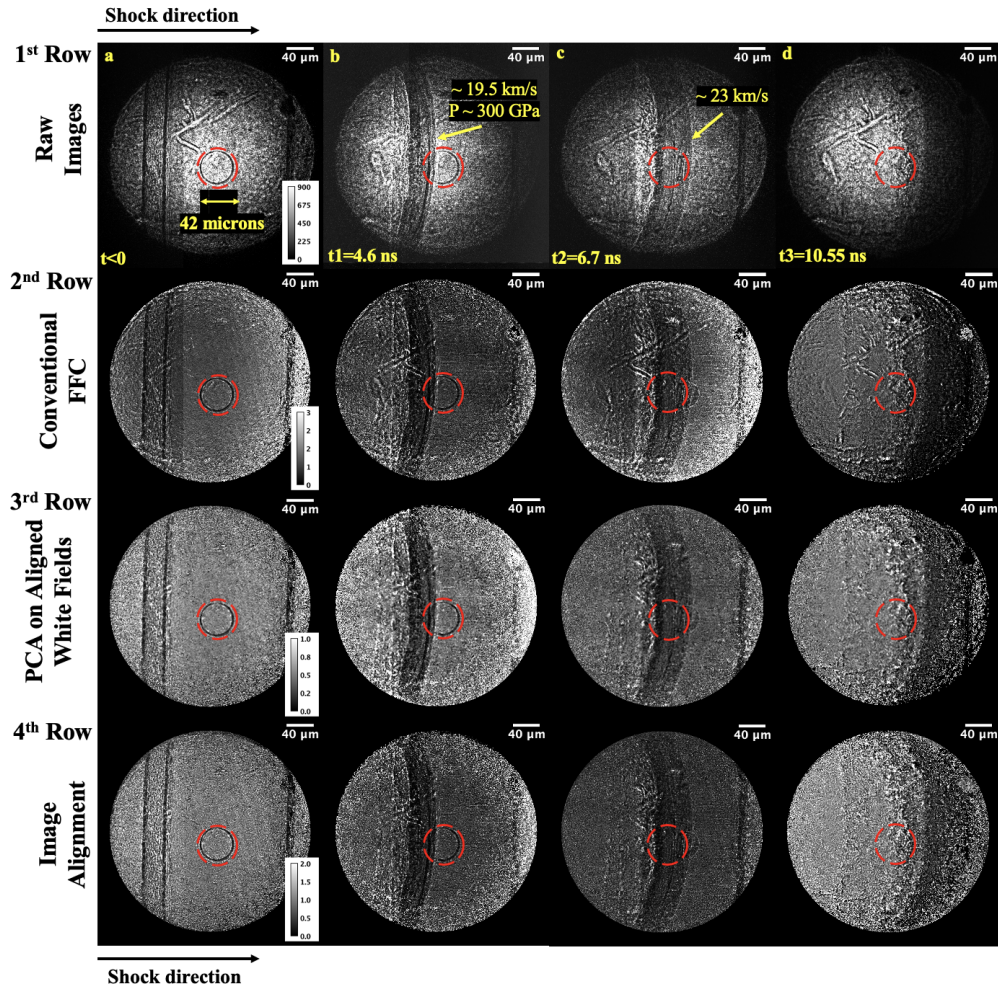


Fig. 5. A 10 ns flat-top pulse was used to shock the sample and images were collected on the UXI detector. Each row contains a sequence of four normalized FFC images of a single sample. For each row, the images are scaled based on the given scale bar in the left panel. The scale bars are given as I/I_0 , where I is the original image and I_0 is the image used to divide and give the normalized flat-field image. The dashed red circles indicate the location of the 42 μm diameter hollow silica void as the shock propagates through the SU-8 material. **First Row (a-d):** Raw images obtained for this experimental campaign. **Second Row:** Conventional flat-field corrected (FFC) images produced by dividing the dynamic images with the average white field. **Third Row:** FFC images generated by applying principal component analysis (PCA) on only the registered white fields generated by the image alignment method. **Fourth Row:** FFC images using only the image alignment method.

projecting the data to lower dimensions, which are interpreted as principal components (PCs). These PCs can be thought of as effective modes of SASE beam fluctuations and instability. A linear combination of all the principal components completely describes the original data set. However, a few components contains a majority of the information from the original data set, so not all components are required for FFC. More components gives higher accuracy, but at the cost of additional computation time.

To account for long term drifts of the XFEL, and to apply proper FFC for sets of dynamic images, we collected white field images prior to every dynamic shot [27]. For selected dynamic runs, we used PCA to search for the maximum variance between the collected white fields, which would indicate major contributing factors to noise and x-ray pulse deviations. PCs are constructed and ordered based on what caused the most variation between each of the white field images, i.e., each component is orthonormal and can be considered an eigenvector pointing in the direction that describes the most variance in the data set. Every eigenvector has an associated eigenvalue, a scalar that reflects the amount of variation that the eigenvector accounts for (higher eigenvalue means higher the variation). Visualization of these components are shown in the supporting information. For example, component one corrects for the intensity variations between pulses, which is known to strongly fluctuate on a shot-to-shot basis for XFELs. The subsequent components account for and correct the pointing stability (center of mass of the beam being shifted between each image), which is another contributing factor that describes the SASE pulses. Therefore, projecting the white fields to lower dimensions with PCA gives a unique representation of what contributes most to XFEL beam behavior, so FFC images can be generated.

The number of PCs chosen for best FFC results are based on two considerations: 1) the number of components cannot exceed the number of white fields obtained, and 2) we kept only the first five principal components since this amount resulted in a majority of the variance and reduced computational time. For our void-shock image sequence, we collected a total of 40 white fields prior to the dynamic shot, but only 27 were used since some white fields were corrupted or had low intensity. For the void-shock image displayed in the bottom row of Fig. 3, we used five principal components accounting for ~96% of the total variation. Images incorporating this technique are shown in the supporting information. Once PCs were obtained, we constructed weights by projecting the dynamic image that needed FFC on the basis given by the components. When the weights were obtained, a synthetic flat-field image was created which is used to normalize our dynamic image. Prior to computing PCA, spurious pixels were replaced by the median value of the image to improve FFC results. Additionally, we set negative pixel values to 0 as they were not physical. To further aid in FFC, we performed image alignment to correct for high frequency variations.

4.1.2. Image alignment

PCA is effective in correcting pulse-to-pulse variations in the x-ray beam intensity. However, the combination of pulse-to-pulse variations in the x-ray beam energy, long-pulse laser shockwave, shift artifacts in the images created from defects in the lenses, which PCA cannot correct. To alleviate this problem, we track the displacement of the high frequency intensity modulations before and after the object is inserted into the optical path. To determine these relative shifts, the diffeomorphic demon's algorithm [28,29] was used to perform a nonrigid image registration between the white fields and dynamic images. This algorithm solves an unconstrained regularized minimization problem by reducing the difference in intensity between the white fields and dynamic images while penalizing for roughness in the displacement field.

For successful FFC we first registered all of our white fields to the first white field event. After that, we formed a single averaged white field image from these aligned fields. The averaged white field were aligned to each dynamic image to compute the displacement field. This was

then applied to the original white fields for each dynamic frame. We divided our dynamic shots with the aligned white fields, generating FFC images shown in the bottom row of Fig. 5.

4.1.3. Combining PCA and image alignment

We combined image alignment and PCA to account and correct for both high- and low-frequency variations. The order in which we applied these techniques was based on a systematic comparison of the image alignment method and PCA on obtained white fields. For the best FFC results, we determined that PCA should be applied after image alignment. For each dynamic frame, the white field images were registered and aligned as described in Section 4.1.2. Furthermore, as described in Section 4.1.1, we performed pixel correction and then used these corrected and registered white fields as our "new" white fields for the PCA algorithm to synthesize FFC images. Here, only five principal components were used, accounting for ~96% of the total variation in this "new" white field data set. These images are shown in the third row in Fig. 5. Overall, the combination of these techniques yield clearer, visible features within the images compared to each method on its own. It should be noted that there are still artifacts present in all the images in Fig. 5 regardless of method because of strong phase-contrast effects distorting the artifacts beyond which can be corrected by using these methods.

4.2. Experimental comparison to XPCI simulations

A void-shock interaction, or generally known as a shock-bubble interaction (SBI), is a standard configuration when analyzing shock-accelerated inhomogeneous flows [54]. Even in this idealized sample configuration, several complex mechanisms occur when a shockwave impacts a void, giving rise to three main processes that occur within the multimaterial medium: compression/acceleration, shock reflection/refraction, and baroclinic vorticity generation [54]. These processes are nonlinearly coupled to each other, forming complicated features based on disordered rotational motion and turbulent mixing that arises during compression. The recent advancement of cameras, such as the ultrafast Icarus V2 camera that we have implemented, enables direct observation of inhomogeneous flow evolution at the nanosecond time scale caused by impulsively driving cavities within ablator materials. Here, we compare our experimental four frame compression of a single sample to its corresponding simulated multi-frame XPCI void-shock images to provide insight into material behavior at the nanosecond and micron scales.

A two-dimensional simulation was performed in xRAGE, a Los Alamos National Laboratory (LANL) Eulerian radiation-hydrodynamics code, to study the effects of shock propagation and instabilities that occur in a single material containing a micro-void. xRAGE is an Eulerian finite volume code that solves the compressible Euler equations with adaptive mesh refinement in 1-, 2-, and 3-dimensions, and SESAME tabular equations of state [55]. Radiation transport and strength effects were neglected in our simulations. We chose specific parameters for this simulation to best match our experimental conditions. The parameters are listed in Table 2 in the supporting information.

This simulation provided a model to help us understand void collapse evolution within the SU-8 medium. A movie of 160 density images with temporal resolution of 0.1 ns was provided, revealing collapse dynamics occurring on timescales shorter than the frame rate of the UXI camera. Density images corresponding to experimental images at similar time frames were inserted into the Supplement 1 for reference. To provide a one-to-one correspondence between experimental data and simulation, we calculated the phase and attenuation maps by performing a forward Abel transform on the simulated density images. Once these maps were generated, we used the angular spectrum method to numerically propagate them a distance L , an effective propagation distance determined in Section 4.3 and the Supplement 1. Among these images, a few were selected based on how well they resembled our experimental data at a specified time interval. Figure 6 shows how closely the XPCI simulation resembles the void-shock evolution

of the experiment. The simulated image in panel (d) was included to explain what we would expect to see experimentally if higher temporal resolution was obtained. Each simulated frame (panels (c)-(e) in Fig. 6) shows progressive movement of the shock front through the void, clearly displaying the void-shock evolution at different time steps. The first simulated frame (panel (c)) at 4 ns is comparable to the experimental image at 4.6 ns (panel (a)), when our shock initially strikes our void. As the shock enters the void, it accelerates, traveling faster than the unperturbed exterior shock. One nanosecond later (panel (d) in Fig. 6), the interior shock reaches the far side of the void, and begins to exit the far side of the bead. At 6 ns in the last simulated frame (panel (e)), corresponding to 6.7 ns experimentally (panel (b)), the remaining bead material has been swept up by the portion of the shock that traversed the void, and some material is now displaced ahead of the oncoming unperturbed shock. The distribution of this bead material is in good agreement with the second frame from the UXI camera (panel (b)). We note that there is an aliasing effect that starts to develop on the left side of Fig. 6(e) and this has insignificant influence when qualitatively comparing simulated and experimental images.

Using the known EOS for polyimide as described in Section 2, we estimate the pressure attained in each experimental image; propagation of a shockwave leads to void compression and results in a jump of pressure, temperature, density, and translational velocity. Translational void velocity is noticeable by comparing the red dashed circles in Figs. 4 and 5. During each time step in Fig. 5, it is seen that the void is displaced from its original location. By examining the purple arrow in Fig. 6(a), we see mass is stripped off the original bubble and mixes with the surrounding heated up fluids. This process continues as the shock wave propagates through the void and ablator material. A purple arrow is also included in corresponding simulated image for comparison (see Fig. 6(c)). Vorticity is seen on the edges of the void in Fig. 6(b), where yellow arrows are used to label the resulting curl up. Yellow arrows are included in the simulated image (see Fig. 6(e)) for comparison to the corresponding experimental image. We generated an average shock speed of $U_s \sim 19.5$ km/s, which corresponds to a pressure of 300 GPa as estimated from the polyimide equation of state [34,56].

4.3. Application of the transport-of-intensity (TIE) based method

The direct-imaging geometry enables images to be recorded in the near-field regime. In this regime, the image provides a "direct" resemblance of the object. In our study, this allows us to visualize both the void and shock front without being masked by large Fresnel fringes and corresponding refractive dark band effects. Furthermore, direct-imaging linearly relates the image intensity and properties of the object. We exploited this relationship by using a TIE based approach to calculate mass density maps of the shock-induced void collapse displayed in Fig. 7.

In comparison to traditional propagation-based near-field imaging geometries, where there are no optics between the sample and detector, direct-imaging has additional layers of complexity when analyzing the images. First, images recorded in the direct-imaging geometry are modified by both propagation-based phase effects and absorption of X-rays in the compound refractive lens. Several works have investigated these effects both theoretically and experimentally [57–60]. In our experimental setup, we employed Be-CRL. This resulted in a differential absorption between the center and edge ($\sim 40 \mu\text{m}$ from the center) of the lens of $\sim 3.5\%$. However, this differential is negligible compared to sample-induced intensity variations. We can therefore use equations describing free-space wave propagation to relate the image intensity to the object wavefield [61]. In this study, we chose the continuity TIE equation and re-derived the single image phase retrieval algorithm developed by Paganin et al. [62] to solve for the average mass density ($\int \rho dz$) of the sample along the direction of the x-ray beam from a single flat-field corrected image I of pixel size W :

$$\frac{\int \rho dz}{T} = -\frac{1}{\mu T} \log \left[F^{-1} \left\{ \frac{F\{I\}}{\frac{2L\delta}{\mu W^2} [\cos(Wk_x) + \cos(Wk_y) - 2]} \right\} \right] \quad (2)$$

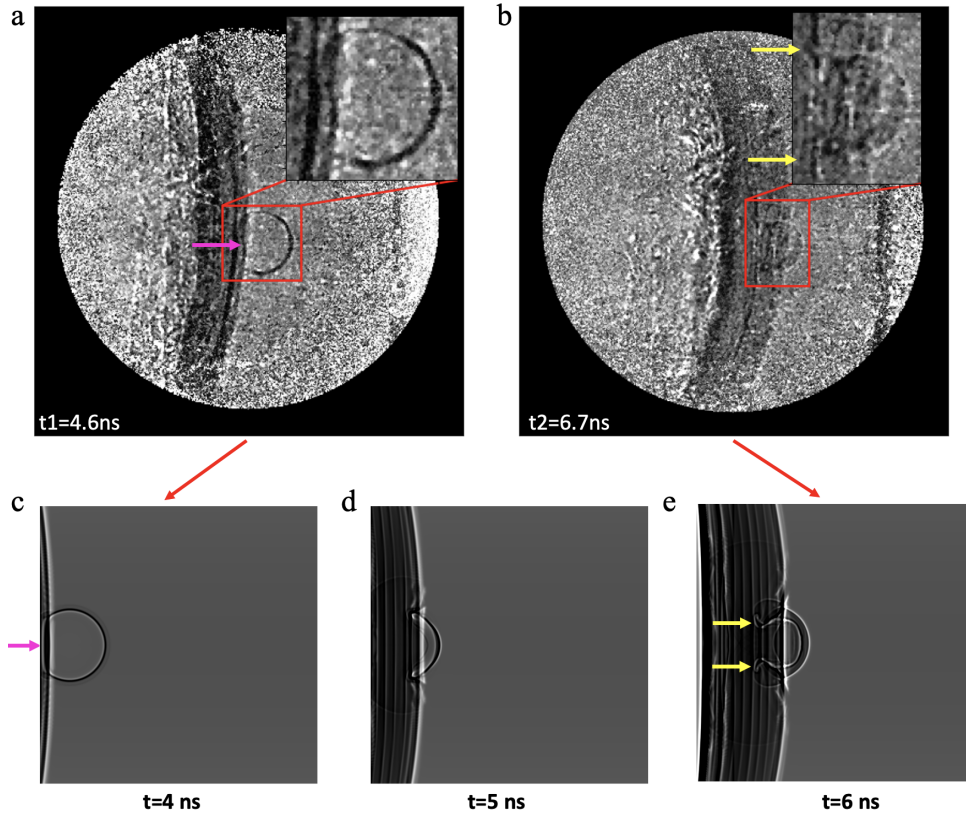


Fig. 6. Top Row: Experimental intensity images capturing void-shock interaction. Panel (a) and panel (b) displays shock propagation 4.6 ns and 6.7 ns (2.1 ns after panel (a)) after the shock wave impacts the medium. The insets in panel a and b show a zoomed in version of the void-shock interaction for better visibility. The purple arrow in panel (a) indicates the mass being stripped off the SiO_2 shell while the yellow arrows in panel (b) indicate the curl up at the edges of the void as a result of the shock wave propagating through it. **Bottom Row:** The red arrows indicate the simulated intensity images that correspond to the experimental intensity images depicted in the top row. Panel (c) shows 4 ns after a shock wave interacts with the medium while panel (e) displays the intensity after 6 ns, corresponding to nearly the same time step experimentally. Panel (d) is an intermediate time step (5 ns) that occurs 1 ns after the first frame. **Note:** We recognize that the void-shock interaction is aligned in simulation, while it is not the case for the experimental images. The experimental misalignment was unintentional and arose due to experimental conditions at the time. However, we attempted to match simulation and experiment as best as possible.

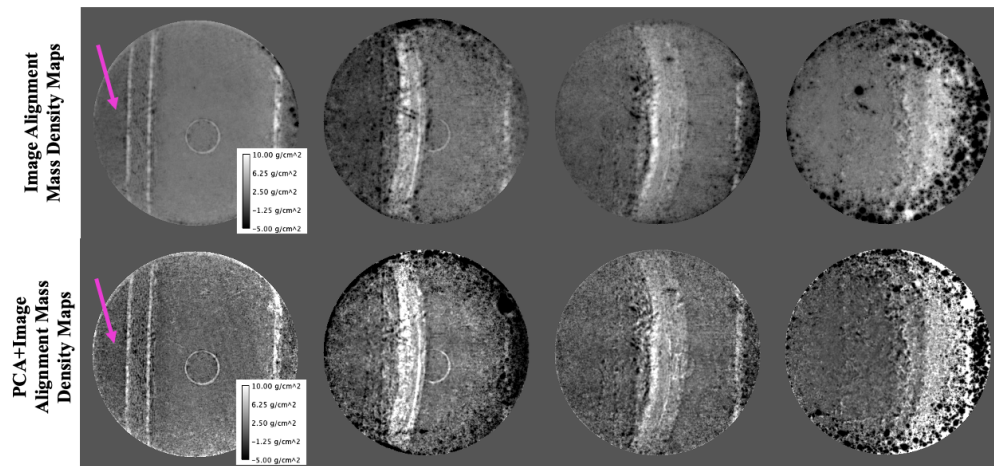


Fig. 7. We use the transport-of-intensity (TIE) based approach to analytically solve for the average projected mass density (areal density) of the multi-material medium containing SU-8 and the hollow SiO₂ void before and during shock compression. These images are still very preliminary. The scale range in the left panels are used for all the images. The purple arrows in the left column indicate portions of the sample which contain air only. Each image was rescaled such that the average mass density (areal density) containing air only is 0. **Top Row:** TIE based approach applied to the image alignment technique. **Bottom Row:** TIE based approach applied to the combination of the PCA and image alignment technique.

In deriving Eq. (2), we assumed spatially coherent, monochromatic x-rays and their interaction with the sample when it obeys the projection approximation. In addition, the sample is composed of a single material with a complex refractive index $1 - \delta\rho + i\mu\rho$, where μ is the mass attenuation coefficient per mass density, δ is the refractive index decrement per mass density. $k_{\perp} = (k_x, k_y)$ is the transverse spatial frequencies in frequency space corresponding to the image real space coordinates (x, y) . These coordinates are related by the Fourier and inverse Fourier transforms, F and F^{-1} , respectively. L presents the distance of the detector from the Be-CRL image plane, which means L can be positive or negative. T is the thickness of the sample along the x-ray propagation direction and is assumed to be constant. We note that although the mass attenuation coefficient changes with temperature, its effect is insignificant unless extreme temperatures are involved. Specifically, for our experiment, changes to the material attenuation coefficients in our warm dense matter regime are no more than 0.1% - 1% for silicon and carbon based on FLYCHK calculations [63] for temperatures of 1–5 eV. Therefore, changes in the material attenuation coefficients are negligible and Eq. (2) remains valid for our experiment.

Directly measuring L is non-trivial because of difficulties in accurately measuring the Be-CRL effective focal and image planes. To overcome this challenge, we performed XPCI simulations using the angular spectrum method of a SiO₂ shell embedded in SU-8 for different L and SiO₂ shell thicknesses. These results are contained in the supporting information. We compared Fig. 5 to these simulated images, and we concluded from the presence of a distinct dark band with bright bands on either side seen in Fig. 5 that $L \geq 0$ mm. This results in much smaller numerical errors as opposed to when L is negative, where there will be a division by zero in Eq. (2). Consequently, L can be tuned within the domain $[0, \infty)$ until the Fresnel fringes in the image are removed and applied to the other images. Also, due to the pulse-to-pulse fluctuation in the x-ray that was not fully corrected with our flat-field correction method, we rescaled each image in Fig. 7 such that the average mass density containing air only (indicated by the arrow in Fig. 7) is zero.

Equation (2) can accurately solve for single material samples, but our sample is composed of two materials, SiO₂ and SU-8. While there are single image multi-material TIE-based phase retrieval algorithms [64], these algorithms assume only one of the materials has spatially varying properties. Therefore, we chose to tune Eq. (2) to calculate the average mass density of SU-8. This allowed us to compare the average mass density of the shock front with the xRAGE simulations. In regions containing the void, it is slightly over-blurred and not quantitatively correct; however, image noise surrounding it was inadvertently suppressed and improves visual comparison with the xRAGE simulations.

Figure 7 shows the average mass density maps of the two methods shown in the bottom rows in Fig. 5. The speckle-only average mass density maps display less high frequency artifacts than that of PCA combined with speckle. However, without PCA there is still low frequency variations present due to imperfect normalization against the stochastically varying x-ray beam intensity profile. We suspect this is because of the small number of white fields that were available for PCA. In future experiments, we plan to record more white fields for PCA before combining with speckle to remove both low- and high-frequency artifacts in the average mass density maps. There are regions in which the average mass density is negative, particularly towards the edge of the x-ray beam where the photon count is low or where portions of the image are noisy after FFC. The TIE assessment presented here is just a preliminary test of this method. In future works, we plan to generalize Eq. (2) to solve for multiple material properties by incorporating advanced model-based iterative reconstruction methods that also account for Poisson noise by, for example, imposing positivity constraints to ρ .

5. Conclusion

The UXI platform demonstrated here has the potential to revolutionize HEDP with the capability to capture multiframe material dynamics of a single sample at the nanosecond time scale. We have successfully captured a series of three dynamic frames of void-shock evolution with 700 nm half-pitch resolution over 8 ns in a direct-imaging geometry. Our results advance our understanding of void collapse in extreme states and demonstrates the wide applicability of the UXI camera. These results provide fundamental insight on how material inhomogeneities, such as micro-voids, influence material properties during the propagation of a laser shockwave. Moreover, to quantitatively understand void-shock interaction and how the material structure evolves over several nanoseconds, we utilized a TIE-based phase retrieval method to give us the average projected mass density of the sample. The UXI has demonstrated that pressure regimes of several Mbar can be imaged, paving the way for understanding physics over shorter time-scales for non-repeatable ultrafast phenomena. Our technique for void characterization during laser shock compression will contribute to minimizing instabilities that occur at the micron scale in ICF experiments.

Next generation gallium arsenide (GaAs) sensors will extend this technique to higher x-ray energies, expanding burst-mode science experiments. Although this detector was designed for HEDP experiments that require nanosecond sampling, it can acquire data at nanosecond or sub-nanosecond time scales, improving data acquisition speed and overall operational efficiency. Moreover, with improvements to the camera, particularly the quantum efficiency, will lead to improved accuracy in quantification of the projected average mass density, enabling us to understand nanosecond time evolution of matter in extreme conditions.

Funding. U.S. Department of Energy (20200744PRD1, 20210717ER, 80NSSC18K0772, DE-AC02-76SF00515, DE-NA0003856, DE-NA0003914, DE-SC0014318 DE-SC0019329, DE-SC0020229, ECCS-2026822, FWP100182, OCE-2123496, PHY-2020249, FES-Early Career Award (2019)).

Acknowledgments. The authors would like to thank the accelerator team at LCLS for providing the four-pulse trains. Also, we would like to thank Johannes Hagemann for his insights and suggestions regarding PCA.

Disclosures. The authors declare no conflicts of interest.

Data availability. Data underlying the results presented in this paper are not publicly available at this time but may be obtained from the authors upon reasonable request.

Supplemental document. See [Supplement 1](#) for supporting content.

References

1. D. Jamison, "Fusion news ignites optimism," *Nature Photonics* 2021 15:10 **15**, 713 (2021).
2. R. Betti and O. A. Hurricane, "Inertial-Confinement fusion with lasers," (2016).
3. J. A. Gaffney, S. T. Brandon, K. D. Humbird, M. K. Kruse, R. C. Nora, J. L. Peterson, and B. K. Spears, "Making inertial confinement fusion models more predictive," *Phys. Plasmas* **26**(8), 082704 (2019).
4. R. S. Craxton, K. S. Anderson, T. R. Boehly, V. N. Goncharov, D. R. Harding, J. P. Knauer, R. L. McCrory, P. W. McKenty, D. D. Meyerhofer, J. F. Myatt, A. J. Schmitt, J. D. Sethian, R. W. Short, S. Skupsky, W. Theobald, W. L. Kruer, K. Tanaka, R. Betti, T. J. Collins, J. A. Delettrez, S. X. Hu, J. A. Marozas, A. V. Maximov, D. T. Michel, P. B. Radha, S. P. Regan, T. C. Sangster, W. Seka, A. A. Solodov, J. M. Sours, C. Stoeckl, and J. D. Zuegel, "Direct-drive inertial confinement fusion: A review," (2015).
5. K. D. Humbird, J. L. Peterson, J. Salmonson, and B. K. Spears, "Cognitive simulation models for inertial confinement fusion: Combining simulation and experimental data," *Phys. Plasmas* **28**(4), 042709 (2021).
6. V. A. Smalyuk, S. V. Weber, D. T. Casey, D. S. Clark, J. E. Field, S. W. Haan, B. A. Hammel, A. V. Hamza, D. E. Hoover, O. L. Landen, A. Nikroo, H. F. Robey, and C. R. Weber, "Hydrodynamic instability growth of three-dimensional, native-roughness modulations in x-ray driven, spherical implosions at the National Ignition Facility," *Phys. Plasmas* **22**(7), 072704 (2015).
7. V. A. Smalyuk, C. R. Weber, O. L. Landen, S. Ali, B. Bachmann, P. M. Celliers, E. Dewald, A. Fernandez, B. A. Hammel, G. Hall, A. G. MacPhee, L. Pickworth, H. F. Robey, N. Alfonso, K. L. Baker, L. F. Hopkins, L. Carlson, D. T. Casey, D. S. Clark, J. Crippen, L. Divol, T. Döppner, J. Edwards, M. Farrell, S. Felker, J. E. Field, S. W. Haan, A. V. Hamza, M. Havre, M. C. Herrmann, W. W. Hsing, S. Khan, J. Kline, J. J. Kroll, S. LePape, E. Loomis, B. J. MacGowan, D. Martinez, L. Masse, M. Mauldin, J. L. Milovich, A. S. Moore, A. Nikroo, A. Pak, P. K. Patel, J. L. Peterson, K. Raman, B. A. Remington, N. Rice, M. Schoff, M. Stadermann, and S. A. Yi, "Recent and planned hydrodynamic instability experiments on indirect-drive implosions on the National Ignition Facility," *High Energy Density Phys.* **36**, 100820 (2020).
8. J. R. Peterson, B. M. Johnson, and S. W. Haan, "Instability growth seeded by DT density perturbations in ICF capsules," *Phys. Plasmas* **25**(9), 092705 (2018).
9. D. S. Clark, M. M. Marinak, C. R. Weber, D. C. Eder, S. W. Haan, B. A. Hammel, D. E. Hinkel, O. S. Jones, J. L. Milovich, P. K. Patel, H. F. Robey, J. D. Salmonson, S. M. Sepke, and C. A. Thomas, "Radiation hydrodynamics modeling of the highest compression inertial confinement fusion ignition experiment from the National Ignition Campaign," *Phys. Plasmas* **22**(2), 022703 (2015).
10. V. A. Thomas and R. J. Kares, "Drive asymmetry and the origin of turbulence in an ICF implosion," *Phys. Rev. Lett.* **109**(7), 075004 (2012).
11. L. A. Pickworth, B. A. Hammel, V. A. Smalyuk, H. F. Robey, L. R. Benedetti, L. Berzak Hopkins, D. K. Bradley, J. E. Field, S. W. Haan, R. Hatarik, E. Hartouni, N. Izumi, S. Johnson, S. Khan, B. Lahmann, O. L. Landen, S. Le Pape, A. G. MacPhee, N. B. Meezan, J. Milovich, S. R. Nagel, A. Nikroo, A. E. Pak, R. Petrasso, B. A. Remington, N. G. Rice, P. T. Springer, M. Stadermann, K. Widmann, and W. Hsing, "Visualizing deceleration-phase instabilities in inertial confinement fusion implosions using an "enhanced self-emission" technique at the National Ignition Facility," *Phys. Plasmas* **25**(5), 054502 (2018).
12. A. B. Zylstra, D. T. Casey, A. Kritcher, L. Pickworth, B. Bachmann, K. Baker, J. Biener, T. Braun, D. Clark, V. Geppert-Kleinrath, M. Hohenberger, C. Kong, S. Le Pape, A. Nikroo, N. Rice, M. Rubery, M. Stadermann, D. Strozzi, C. Thomas, P. Volegov, C. Weber, C. Wild, C. Wilde, D. A. Callahan, and O. A. Hurricane, "Hot-spot mix in large-scale HDC implosions at NIF," *Phys. Plasmas* **27**(9), 092709 (2020).
13. B. M. Haines, J. P. Sauppe, B. J. Albright, W. S. Daughton, S. M. Finnegan, J. L. Kline, and J. M. Smidt, "A mechanism for reduced compression in indirectly driven layered capsule implosions," *Phys. Plasmas* **29**(4), 042704 (2022).
14. S. Pandolfi, T. Carver, D. Hodge, A. F. Leong, K. Kurzer-Ogul, P. Hart, E. Galtier, D. Khaghani, E. Cunningham, B. Nagler, H. J. Lee, C. Bolme, K. Ramos, K. Li, Y. Liu, A. Sakdinawat, S. Marchesini, P. M. Kozlowski, C. B. Curry, F.-J. Decker, S. Vetter, J. Shang, H. Aluie, M. Dayton, D. S. Montgomery, R. L. Sandberg, and A. E. Gleason, "Novel Fabrication Tools for Dynamic Compression Targets with Engineered Voids Using Photolithography Methods," *Rev. Sci. Instrum.* (2022).
15. L. Claus, L. Fang, R. Kay, M. Kimmel, J. Long, G. Robertson, M. Sanchez, J. Stahoviak, D. Trotter, and J. L. Porter, "An overview of the Ultrafast X-ray Imager (UXI) program at Sandia Labs," in *Target Diagnostics Physics and Engineering for Inertial Confinement Fusion IV*, vol. 9591 (2015).
16. L. D. Claus, M. Sanchez, G. A. Robertson, J. L. Porter, L. Fang, D. Trotter, T. England, A. C. Carpenter, M. S. Dayton, and P. Bhogilal, "Design and characterization of an improved 2 ns multi-frame imager for the ultra-fast x-ray imager (UXI) program at Sandia National Laboratories," (2017).
17. Q. Looker, A. P. Colombo, M. Kimmel, and J. L. Porter, "X-ray characterization of the Icarus ultrafast x-ray imager," *Rev. Sci. Instrum.* **91**(4), 043502 (2020).

18. E. R. Hurd, A. C. Carpenter, M. S. Dayton, C. E. Durand, L. D. Claus, K. Engelhorn, M. O. Sanchez, and S. R. Nagel, "Performance characterization of a four-frame nanosecond gated hybrid CMOS image sensor," (2018).
19. E. R. Hurd, T. Tate, M. S. Dayton, L. D. Claus, C. E. Durand, M. Johnston, J.-M. G. Di Nicola, A. C. Carpenter, and M. O. Sanchez, "Time Resolved Near Field (TRNF) diagnostic four-frame nanosecond gated hybrid CMOS image sensor," (2019).
20. P. A. Hart, A. C. Carpenter, L. D. Claus, D. S. Damiani, M. S. Dayton, F.-J. Decker, A. Gleason, P. A. Heimann, E. Hurd, E. McBride, S. Nelson, M. O. Sanchez, S. Song, and D. Zhu, "First x-ray test of the Icarus nanosecond-gated camera," (2019).
21. B. Nagler, B. Arnold, G. Bouchard, R. F. Boyce, R. M. Boyce, A. Callen, M. Campell, R. Curiel, E. Galtier, J. Garofoli, E. Granados, J. Hastings, G. Hays, P. Heimann, R. W. Lee, D. Milathianaki, L. Plummer, A. Schropp, A. Wallace, M. Welch, W. White, Z. Xing, J. Yin, J. Young, U. Zastrau, and H. J. Lee, "The Matter in Extreme Conditions instrument at the Linac Coherent Light Source," *J. Synchrotron Radiat.* **22**(3), 520–525 (2015).
22. B. Nagler, A. Schropp, E. C. Galtier, B. Arnold, S. B. Brown, A. Fry, A. Gleason, E. Granados, A. Hashim, J. B. Hastings, D. Samberg, F. Seiboth, F. Tavella, Z. Xing, H. J. Lee, and C. G. Schroer, "The phase-contrast imaging instrument at the matter in extreme conditions endstation at LCLS," *Rev. Sci. Instrum.* **87**(10), 103701 (2016).
23. A. Aquila, A. Barty, C. Bostedt, S. Boutet, G. Carini, D. DePonte, P. Drell, S. Doniach, K. H. Downing, T. Earnest, H. Elmlund, V. Elser, M. Gühr, J. Hajdu, J. Hastings, S. P. Hau-Riege, Z. Huang, E. E. Lattman, F. R. Maia, S. Marchesini, A. Ourmazd, C. Pellegrini, R. Santra, I. Schlichting, C. Schroer, J. C. Spence, I. A. Vartanyants, S. Wakatsuki, W. I. Weis, and G. J. Williams, "The linac coherent light source single particle imaging road map," *Struct. Dyn.* **2**(4), 041701 (2015).
24. A. Schropp, R. Hoppe, V. Meier, J. Patommel, F. Seiboth, H. J. Lee, B. Nagler, E. C. Galtier, B. Arnold, U. Zastrau, J. B. Hastings, D. Nilsson, F. Uhlén, U. Vogt, H. M. Hertz, and C. G. Schroer, "Full spatial characterization of a nanofocused X-ray free-electron laser beam by ptychographic imaging," *Sci. Rep.* **3**(1), 1633 (2013).
25. A. Schropp, R. Hoppe, V. Meier, J. Patommel, F. Seiboth, Y. Ping, D. G. Hicks, M. A. Beckwith, G. W. Collins, A. Higginbotham, J. S. Wark, H. J. Lee, B. Nagler, E. C. Galtier, B. Arnold, U. Zastrau, J. B. Hastings, and C. G. Schroer, "Imaging Shock Waves in Diamond with Both High Temporal and Spatial Resolution at an XFEL," *Sci. Rep.* **5**(1), 11089 (2015).
26. H. Chen, N. Palmer, M. Dayton, A. Carpenter, M. B. Schneider, P. M. Bell, D. K. Bradley, L. D. Claus, L. Fang, T. Hilsabeck, M. Hohenberger, O. S. Jones, J. D. Kilkenny, M. W. Kimmel, G. Robertson, G. Rochau, M. O. Sanchez, J. W. Stahoviak, D. C. Trotter, and J. L. Porter, "A high-speed two-frame, 1-2 ns gated X-ray CMOS imager used as a hohlraum diagnostic on the National Ignition Facility (invited)," *Rev. Sci. Instrum.* **87**(11), 11E203 (2016).
27. J. Hagemann, M. Vassholz, H. Hoeppe, M. Osterhoff, J. M. Rosselló, R. Mettin, F. Seiboth, A. Schropp, Johannes Möller, Jörg Hallmann, C. Kim, M. Scholz, U. Boesenberg, R. Schaffer, A. Zozulya, W. Lu, R. Shayduk, A. Madsen, C. G. Schroera, and T. Salditt, "Single-pulse phase-contrast imaging at free-electron lasers in the hard X-ray regime," *J. Synchrotron Radiat.* **28**(1), 52–63 (2021).
28. T. Vercauteren, X. Pennec, A. Perchant, and N. Ayache, "Non-parametric diffeomorphic image registration with the demons algorithm," in *Lecture Notes in Computer Science (including subseries Lecture Notes in Artificial Intelligence and Lecture Notes in Bioinformatics)*, vol. 4792, (2007).
29. X. Pennec, P. Cachier, and N. Ayache, "Understanding the "demon's algorithm": 3D non-rigid registration by gradient descent," in *Lecture Notes in Computer Science (including subseries Lecture Notes in Artificial Intelligence and Lecture Notes in Bioinformatics)* vol. 1679 (1999).
30. D. Paganin, S. C. Mayo, T. E. Gureyev, P. R. Miller, and S. W. Wilkins, "Simultaneous phase and amplitude extraction from a single defocused image of a homogeneous object," *J. Microsc.* **206**(1), 33–40 (2002).
31. M. Beltran, D. Paganin, K. Uesugi, and M. Kitchen, "2D and 3D X-ray phase retrieval of multi-material objects using a single defocus distance," *Opt. Express* **18**(7), 6423 (2010).
32. J. M. Shaw, J. D. Gelorme, N. C. LaBianca, W. E. Conley, and S. J. Holmes, "Negative photoresists for optical lithography," *IBM J. Res. Dev.* **41**(1.2), 81–94 (1997).
33. I. Roch, P. Bidaud, D. Collard, and L. Buchaillot, "Fabrication and characterization of an SU-8 gripper actuated by a shape memory alloy thin film," *J. Micromech. Microeng.* **13**(2), 330–336 (2003).
34. S. Marsh, *LASL Shock Hugoniot Data* (University of California Press, 1980).
35. D. Hodge, S. Pandolfi, Y. Liu, K. Li, A. Sakdinawat, M. Seaberg, P. Hart, E. Galtier, D. Khaghani, S. Vetter, F. J. Decker, B. Nagler, H. J. Lee, C. Bolme, K. Ramos, P. M. Kozlowski, D. S. Montgomery, T. Carver, M. Dayton, L. Dresselhaus-Marais, S. Ali, R. L. Sandberg, and A. Gleason, "Four-frame ultrafast radiography of a shocked sample at an x-ray free electron laser," in *Optics InfoBase Conference Papers*, (2021).
36. F. J. Decker, R. Akre, A. Brachmann, Y. Ding, D. Dowell, P. J. Emma, A. Fisher, J. Frisch, S. Gilevich, P. Hering, Z. Huang, R. Iverson, H. Loos, M. Messerschmidt, H. D. Nuhn, D. Ratner, W. F. Schlotter, T. Smith, J. L. Turner, J. Welch, W. White, and J. Wu, "A demonstration of multi-bunch operation in the LCLS," in *FEL 2010 - 32nd International Free Electron Laser Conference*, (2010).
37. F. J. Decker, K. L. Bane, W. Colocho, S. Gilevich, A. Marinelli, J. C. Sheppard, J. L. Turner, J. J. Turner, S. L. Vetter, A. Halavanau, C. Pellegrini, and A. A. Lutman, "Tunable x-ray free electron laser multi-pulses with nanosecond separation," *Sci. Rep.* **12**(1), 3253 (2022).
38. C. Bostedt, S. Boutet, D. M. Fritz, Z. Huang, H. J. Lee, H. T. Lemke, A. Robert, W. F. Schlotter, J. J. Turner, and G. J. Williams, "Linac Coherent Light Source: The first five years," *Rev. Mod. Phys.* **88**(1), 015007 (2016).

39. B. W. Mcneil and N. R. Thompson, "X-ray free-electron lasers," (2010).
40. P. Emma, R. Akre, J. Arthur, R. Bionta, C. Bostedt, J. Bozek, A. Brachmann, P. Bucksbaum, R. Coffee, F. J. Decker, Y. Ding, D. Dowell, S. Edstrom, A. Fisher, J. Frisch, S. Gilevich, J. Hastings, G. Hays, P. Hering, Z. Huang, R. Iverson, H. Loos, M. Messerschmidt, A. Miahnahri, S. Moeller, H. D. Nuhn, G. Pile, D. Ratner, J. Rzepiela, D. Schultz, T. Smith, P. Stefan, H. Tompkins, J. Turner, J. Welch, W. White, J. Wu, G. Yocky, and J. Galayda, "First lasing and operation of an ångstrom-wavelength free-electron laser," *Nat. Photonics* **4**(9), 641–647 (2010).
41. N. Huang, H. Deng, B. Liu, D. Wang, and Z. Zhao, "Features and futures of X-ray free-electron lasers," *Innovation* **2**(2), 100097 (2021).
42. D. Damiani, M. Dubrovin, I. Gaponenko, W. Kroeger, T. J. Lane, A. Mitra, C. P. O'Grady, A. Salnikov, A. Sanchez-Gonzalez, D. Schneider, and C. H. Yoon, "Linac Coherent Light Source data analysis using psana," *J. Appl. Crystallogr.* **49**(2), 672–679 (2016).
43. B. Pfau and S. Eisebitt, "X-ray holography," in *Synchrotron Light Sources and Free-Electron Lasers: Accelerator Physics, Instrumentation and Science Applications*, (2020).
44. S. C. Mayo, A. W. Stevenson, and S. W. Wilkins, "In-Line Phase-Contrast X-ray Imaging and Tomography for Materials Science," *Materials* **5**(12), 937–965 (2012).
45. M. Endrizzi, "X-ray phase-contrast imaging," *Nucl. Instrum. Methods Phys. Res., Sect. A* **878**, 88–98 (2018).
46. E. Pagot, P. Cloetens, S. Fiedler, A. Bravin, P. Coan, J. Baruchel, J. Härtwig, and W. Thomlinson, "A method to extract quantitative information in analyzer-based x-ray phase contrast imaging," *Appl. Phys. Lett.* **82**(20), 3421–3423 (2003).
47. A. Momose, "Phase-sensitive imaging and phase tomography using X-ray interferometers," *Opt. Express* **11**(19), 2303 (2003).
48. S. B. Brown, A. E. Gleason, E. Galtier, A. Higginbotham, B. Arnold, A. Fry, E. Granados, A. Hashim, C. G. Schroer, A. Schropp, F. Seiboth, F. Tavella, Z. Xing, W. Mao, H. J. Lee, and B. Nagler, "Direct imaging of ultrafast lattice dynamics," *Sci. Adv.* **5**(3), eaau8044 (2019).
49. S. V. Milton, E. Gluskin, N. D. Arnold, C. Benson, W. Berg, S. G. Biedron, M. Borland, Y. C. Chae, R. J. Dejus, P. K. Den Hartog, B. Deriy, M. Erdmann, Y. I. Eidelman, M. W. Hahne, Z. Huang, K. J. Kim, J. W. Lewellen, Y. Li, A. H. Lumpkin, O. Makarov, E. R. Moog, A. Nassiri, V. Sajaev, R. Soliday, B. J. Tieman, E. M. Trakhtenberg, G. Travish, I. B. Vasserman, N. A. Vinokurov, X. J. Wang, G. Wiemerslage, and B. X. Yang, "Exponential gain and saturation of a self-amplified spontaneous emission free-electron laser," *Science* **292**(5524), 2037–2041 (2001).
50. K. Buakar, Y. Zhang, Š. Birnštejnová, V. Bellucci, T. Sato, H. Kirkwood, A. P. Mancuso, P. Vagovic, and P. Villanueva-Perez, "Shot-to-shot flat-field correction at X-ray free-electron lasers," *Opt. Express* **30**(7), 10633–10644 (2022).
51. I. T. Jolliffe and J. Cadima, "Principal component analysis: A review and recent developments," *Phil. Trans. R. Soc. A* **374**(2065), 20150202 (2016).
52. J. Shlens, "A tutorial on principal component analysis: derivation, discussion and singular value decomposition," Online Note <http://www.snl.salk.edu/shlens/pubnotes/pca.pdf> **2**, (2003).
53. L. I. Smith, "A tutorial on Principal Components Analysis Introduction," *Statistics* (2002).
54. D. Ranjan, J. Oakley, and R. Bonazza, "Shock-bubble interactions," *Annu. Rev. Fluid Mech.* **43**(1), 117–140 (2011).
55. M. Gittings, R. Weaver, M. Clover, T. Betlach, N. Byrne, R. Coker, E. Dendy, R. Hueckstaedt, K. New, W. R. Oakes, D. Ranta, and R. Stefan, "The RAGE radiation-hydrodynamic code," *Comput Sci Disc.* **1**(1), 015005 (2008).
56. M. A. Barrios, D. G. Hicks, T. R. Boehly, D. E. Fratanduono, J. H. Eggert, P. M. Celliers, G. W. Collins, and D. D. Meyerhofer, "High-precision measurements of the equation of state of hydrocarbons at 1–10 Mbar using laser-driven shock waves," *Phys. Plasmas* **17**(5), 056307 (2010).
57. C. G. Schroer, B. Benner, T. F. Günzler, M. Kuhlmann, C. Zimprich, B. Lengeler, C. Rau, T. Weitkamp, A. Snigirev, I. Snigireva, and J. Appenzeller, "High resolution imaging and lithography with hard x rays using parabolic compound refractive lenses," *Rev. Sci. Instrum.* **73**(3), 1640–1642 (2002).
58. T. Weitkamp, C. Rau, A. A. Snigirev, B. Benner, T. F. Guenzler, M. Kuhlmann, and C. G. Schroer, "In-line phase contrast in synchrotron-radiation microradiography and tomography," *Developments in X-Ray Tomography III* **4503**, 92–102 (2002).
59. V. Kohn, I. Snigireva, and A. Snigirev, "Diffraction theory of imaging with X-ray compound refractive lens," *Opt. Commun.* **216**(4–6), 247–260 (2003).
60. V. G. Kohn, "An exact theory of imaging with a parabolic continuously refractive X-ray lens," *J. Exp. Theor. Phys.* **97**(1), 204–215 (2003).
61. D. M. Paganin, *Coherent X-Ray Optics* (2006).
62. D. M. Paganin, V. Favre-Nicolin, A. Mirone, A. Rack, J. Villanova, M. P. Olbinado, V. Fernandez, J. C. da Silva, and D. Pelliccia, "Boosting spatial resolution by incorporating periodic boundary conditions into single-distance hard-x-ray phase retrieval," *J. Opt.* **22**, 115607 (2020).
63. H. K. Chung, M. H. Chen, W. L. Morgan, Y. Ralchenko, and R. W. Lee, "FLYCHK: Generalized population kinetics and spectral model for rapid spectroscopic analysis for all elements," *High Energy Density Phys.* **1**(1), 3–12 (2005).
64. I. Häggmark, W. Vågberg, H. M. Hertz, and A. Burvall, "Comparison of quantitative multi-material phase-retrieval algorithms in propagation-based phase-contrast X-ray tomography," *Opt. Express* **25**(26), 33543 (2017).